# Spatially Resolved Optical Emission Spectroscopy Monitoring of Trace Xenon in an Atmospheric-Pressure Helium Microdischarge

Changsu Kim[a], Changwha Lee[a], June Young Kim[b], Geunwoo Go[a, c]*

[a]*Research & Development Team, X-sentry Co., Ltd., 775, Gyeongin-ro, Yeongdeungpo-gu, Seoul 07299, Republic of Korea*
[b]*Department of Semiconductor Engineering, Myongji University, 116, Myongji-ro, Cheoin-gu, Yongin-si, Gyeonggi-do, 17058, Republic of Korea*
[c]*Department of Nuclear Engineering, Seoul National University, 1 Gwanak-ro, Gwanak-gu, Seoul 08826, Republic of Korea*

**Corresponding author: gwgo@x-sentry.com*

***Keywords :** fission gas monitoring, microplasma, optical emission spectroscopy, spatially resolved diagnostics, limit of detection

## 1. Introduction

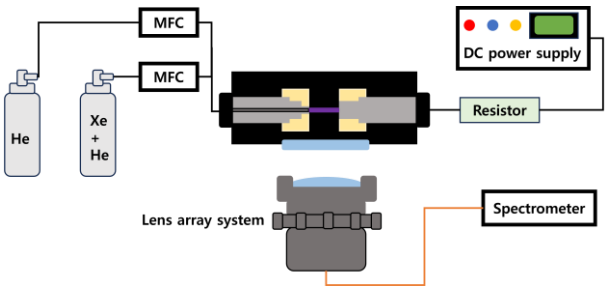
Small modular reactors (SMRs) are emerging as a solution for carbon-neutral energy production, but their economic case rests on factory fabrication, reduced staffing, and simplified operation and maintenance [1,2]. This extends to the instrumentation: monitoring systems must be correspondingly compact, inexpensive, and autonomous. Continuous monitoring of fission gases, particularly xenon and krypton, is essential for fuel-integrity assessment and off-gas management [3]. The need is most explicit in molten salt reactors (MSRs), where noble gases are continuously stripped from the circulating fuel salt by helium sparging and routed through the off-gas system to decay and adsorption beds, a design lineage dating to the MSRE [3,4]. The resulting off-gas is thus a helium stream carrying trace Xe and Kr, precisely the gas matrix addressed in this work. Optical approaches such as laser-induced breakdown spectroscopy have demonstrated real-time detection of noble gases in surrogates of such streams [5]. Atmospheric-pressure glow-discharge emission spectroscopy offers a compact and inexpensive alternative: a stable He microdischarge sustained in the sampled gas stream converts trace Xe into characteristic line emission, so that the Xe content can be quantified in real time from the ratio of Xe to He line intensities.

In such compact discharges, however, the emission is strongly inhomogeneous along the inter-electrode axis: bright near-electrode glows and a weaker mid-gap column coexist within a millimeter-scale gap, and the analyte and carrier lines do not share exactly the same spatial distribution. A line of sight (LOS) integrating the whole discharge light therefore mixes the optical signals of plasma regions with different sensitivity and stability. In this work, a narrow (~0.1 mm) LOS is scanned along the axis of a He microdischarge (1.7 mm gap) in 0.25 mm steps to measure position-resolved spectra for optimal LOS placement and to quantify (i) the Xe I 823.2 nm and He I 706.5 nm intensities and their ratio, (ii) the Xe calibration over 0–500 ppm, and (iii) the stability (RSD).

## 2. Methods

### *2.1. Microdischarge Xe monitoring system*

The microdischarge cell and gas-handling system are shown schematically in Fig. 1. High-purity He (99.999%) and a certified Xe/He mixture were metered by mass flow controllers (Alicat MCS-1SLPM) to synthesize Xe concentrations of 100–500 ppm at a total flow of 600 sccm. The chamber pressure was 102.5 kPa at room temperature. The cathode is designed as a hollow tungsten pin (OD 0.8 mm, bore 0.5 mm) through which the gas is injected, sheathed in a hole-aligned AlN cover to limit the discharge path. The anode is a tungsten rod (OD 2.0 mm) with a BN cover, facing the cathode at a 1.7 mm gap inside a PEEK-lined chamber. A DC supply ignites the discharge at 3 kV and sustains it in constant-current mode at 1.5 mA through a 200 kΩ ballast, with the discharge voltage settling to 500–600 V. These conditions produce a stable glow-mode microdischarge across the gap.



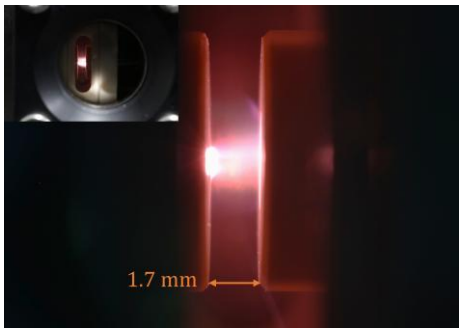



Fig. 1. Schematic of the microdischarge Xe monitoring system (top) and a side-view photograph of the He microdischarge between the hollow-cathode pin and the anode with a 1.7 mm gap (bottom).

### *2.2. Spatially resolved optical detection*

Position-resolved spectra were collected through a two-lens fiber-coupling relay viewing the discharge side-on through the chamber viewport: an objective lens (f = 45 mm) placed 45 mm from the discharge axis, a 0.9-mm-diameter aperture stop, and a fiber-coupling lens (f = 100 mm) focusing onto a 200 μm-core optical fiber. This geometry gives an LOS width of ≈0.1 mm at the discharge, which sets the axial spatial resolution and is finer than the 0.25 mm scan step. The depth of field of ±4.5 mm ensures that each spectrum samples the full column chord at a single axial position. The optics are mounted on a cross-roller stage (10 μm resolution) and scanned along the axis in 0.25 mm steps over 12 positions. Axial positions are quoted relative to the start of the effective sensing range (x = 0), and the luminous column spans ≈1.6–1.7 mm within the scanned range, consistent with the electrode gap. The fiber feeds a compact CMOS spectrometer (Avantes AvaSpec-NXS2048CL-VA, 2048 pixels, 25 μm entrance slit, 348–901 nm), whose instrumental FWHM measured in situ from a Voigt fit of He I 728.1 nm is 0.4–0.7 nm. Spectra were recorded at a sampling interval of 1 s with an integration time of 0.8 s and no on-board averaging, giving ~180 spectra per position and concentration.

### *2.3. Calibration and stability analysis*

At each LOS position, calibration spectra were acquired at fixed Xe concentrations from 0 to 500 ppm in 100 ppm steps. The concentration indicator was defined by the fixed intensity ratio R = I(Xe 823.2)/I(He 706.5), where each line intensity is the background-subtracted area integrated over an effective spectral width of ±1.5 times the Voigt-fitted FWHM of the line. He I 706.5 nm was selected as the reference line because it remains intense and spectrally stable at every LOS position, including the weak mid-gap region. The calibration curve at each position was obtained by linear regression of concentration against the time-averaged ratio over the full 0–500 ppm range, and the statistical performance metrics, the within-plateau RSD and the detection limit LOD = $3\sigma_{blank}$/slope, were defined for concentrations of 100 ppm and above.

## 3. Results and Discussion

### *3.1. Axial structure of the emission*

Fig. 2 shows the position-averaged Xe/He ratio and the Xe I 823.2 and He I 706.5 nm line intensities at every LOS position for 100–500 ppm. The He emission exhibits two maxima adjacent to the electrodes (negative glow and anode glow) separated by a weaker mid-gap column, whereas the Xe emission and the Xe/He ratio peak in the mid-gap region (x ≈ 0.50–0.75 mm), reflecting the different excitation channels of the two species. The Xe emission is fed by low-threshold channels, namely direct electron-impact excitation at 8–11 eV and energy transfer from He metastables (19.8 eV) that are consumed by Xe within tens of micrometers at atmospheric pressure. In contrast, He I 706.5 nm requires 22.7 eV. In the weakly sustained mid-gap column, the softened electron energy distribution therefore suppresses the high-threshold He emission far more strongly than the Xe channels, so the ratio peaks where the He emission is weakest.

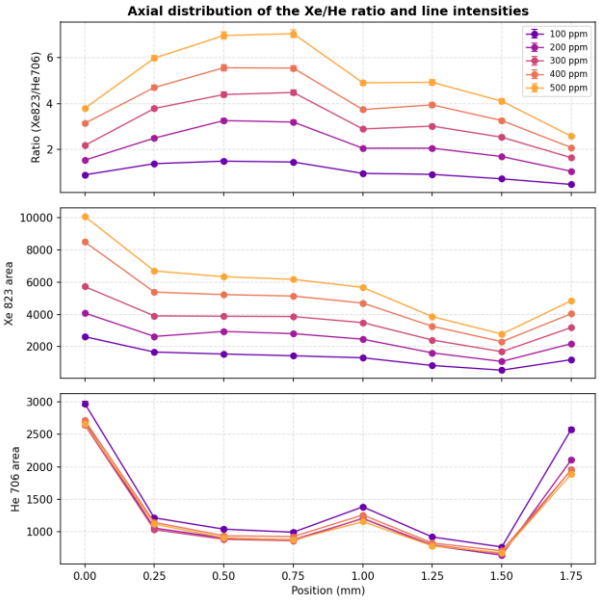



Fig. 2. Axial distribution of the position-averaged Xe/He ratio and the Xe 823 nm and He 706 nm line intensities for 100–500 ppm Xe. Points show the position mean ±1σ of the time series and colors denote the Xe concentration.

### *3.2. Position-resolved calibration performance*

Fig. 3 maps the within-plateau RSD of the ratio over the position–concentration plane. Mid-gap positions maintain an RSD of 1.9–2.8%, while the outermost positions, dominated by electrode-glow stray light, degrade markedly and are excluded from the sensing range. Fig. 4 shows the axial profiles of the calibration slope and $R^2$ over the full 0–500 ppm range. The linearity is uniformly high, with $R^2 \geq 0.995$ at every effective

position (0–1.75 mm), so the position dependence of the sensing characteristics is carried almost entirely by the slope. The slope varies by a factor of ≈2.7 (71.5–191 ppm per unit ratio), with the highest sensitivity (smallest slope) in the mid-gap region (0.50–0.75 mm). Fig. 5 contrasts the calibration curves at the best and worst positions ($R^2$ = 0.9991 at x = 1.25 mm and 0.9950 at x = 0.50 mm). Even the worst-linearity position, which is also the most sensitive one, remains well within calibration-grade linearity. The LOD ($3\sigma_{blank}$/slope) is ≈1 ppm at the mid-gap optimum and 0.8–1.9 ppm across the effective range.

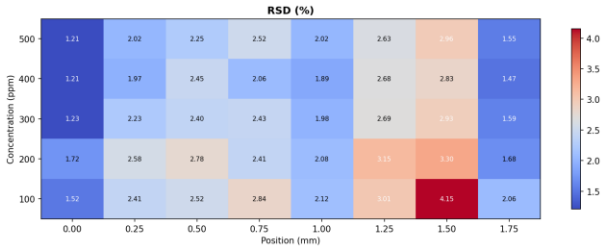



Fig. 3. RSD (%) of the Xe/He ratio as a function of axial position and Xe concentration.

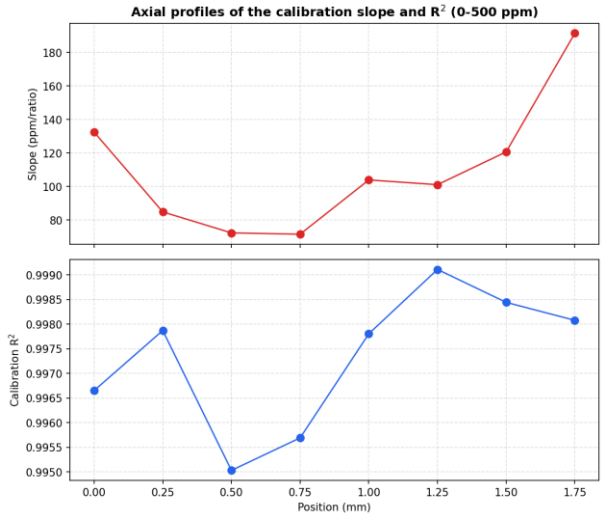



Fig. 4. Axial profiles of the calibration slope (top) and $R^2$ (bottom) for the 0–500 ppm calibration.

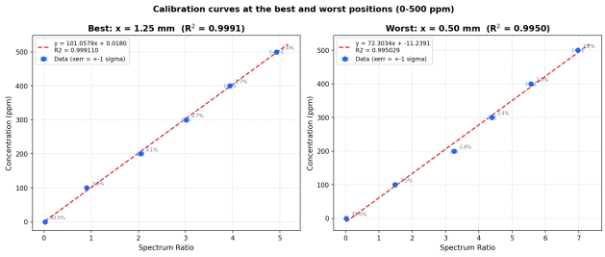



Fig. 5. Calibration curves at the best (x = 1.25 mm) and worst (x = 0.50 mm) positions. Error bars are ±1σ of the time series and labels give the within-plateau RSD.

### *3.3. Implications for monitor design*

The strong axial dependence implies that an integrated-LOS monitor under-utilizes the discharge. Restricting the collection volume to the mid-gap region (x ≈ 0.50–0.75 mm) improves the calibration sensitivity and RSD relative to near-electrode collection while relaxing alignment tolerance. This provides a quantitative basis for fixing the optical design of compact fission-gas monitors without per-device recalibration.

## 4. Conclusion

Spatially resolved emission spectroscopy of a 1.7 mm He microdischarge shows that trace-Xe sensing performance is governed by the axial discharge structure. The Xe I 823.2 / He I 706.5 nm ratio is most sensitive, highly linear ($R^2 \geq 0.995$), and most stable (RSD <3%) when the LOS samples the mid-gap column, where the ratio and the calibration sensitivity both peak and the LOD reaches ≈1 ppm. The position-resolved calibration maps define the optimal collection geometry for low-cost SMR fission-gas monitors and support extension to Kr and mixed fission-gas streams.

## Acknowledgments

This work was supported by the Ministry of SMEs and Startups (TIPS program) (No. RS-2025-25461640)

## REFERENCES

[1] NEA, Small Modular Reactors: Challenges and Opportunities, NEA No. 7560, OECD Publishing, Paris, 2021.
[2] B. Mignacca, G. Locatelli, Economics and Finance of Small Modular Reactors: A Systematic Review and Research Agenda, Renewable and Sustainable Energy Reviews, Vol. 118, 109519, 2020.
[3] H. B. Andrews, J. McFarlane, A. S. Chapel, et al., Review of Molten Salt Reactor Off-Gas Management Considerations, Nuclear Engineering and Design, Vol. 385, 111529, 2021.
[4] J. McFarlane, P. A. Taylor, D. E. Holcomb, W. P. Poore, Fission Product Volatility and Off-Gas Systems for Molten Salt Reactors, ORNL/TM-2019/1266, Oak Ridge National Laboratory, Oak Ridge, TN, 2019.
[5] H. B. Andrews, J. McFarlane, K. G. Myhre, Monitoring Noble Gases (Xe and Kr) and Aerosols (Cs and Rb) in a Molten Salt Reactor Surrogate Off-Gas Stream Using Laser-Induced Breakdown Spectroscopy (LIBS), Applied Spectroscopy, Vol. 76, pp. 988-997, 2022.